Epitaxy and Shape Heterogeneity of a Nanoparticle Ensemble during Redox Cycles

Simon Chung,[*,†] Jan-Christian Schober,[†,‡] Steffen Tober,[†,‡] Daniel Schmidt,[‡]
Azat Khadiev,[¶] Dmitri V. Novikov,[¶] Vedran Vonk,[†] and Andreas Stierle[†,‡]

†*CXNS – Center for X-ray and Nano Science, Deutsches Elektronen-Synchrotron DESY, Notkestr. 85, 22607 Hamburg, Germany*

‡*Fachbereich Physik, Universität Hamburg, Jungiusstr. 11, 20355 Hamburg, Germany*

¶*Deutsches Elektronen-Synchrotron DESY, Notkestr. 85, 22607 Hamburg, Germany*

E-mail: simon.chung@desy.de

Abstract

The role of metal-support epitaxy on shape and size heterogeneity of nanoparticles and their response to gas atmospheres is not very well explored. Here we show that an ensemble of Pd nanoparticles, grown on MgO(001) by deposition in ultra-high vacuum, mostly consists of two distinctly epitaxially oriented particles, each having a different structural response to redox cycles. X-ray reciprocal space patterns were acquired *in situ* under oxidizing and reducing environments. Each type of nanoparticle has a truncated octahedral shape, whereby the majority grows with a cube-on-cube epitaxy on the substrate. Less frequently occurring and larger particles have their principal crystal axes rotated $\pm 3.7^\circ$ with respect to the substrate's. Upon oxidation, the top (001) facets of both types of particles shrink. The relative change of the rotated particles' top facets is much more pronounced. This finding indicates that a larger mass transfer is involved for the rotated particles and that a larger portion of high index facets forms. On the main facets of the cube-on-cube particles, the oxidation process results in a considerable strain, as concluded from the evolution to largely asymmetric facet scattering signals. The shape and strain responses are reversible upon reduction, either by annealing to 973 K in vacuum or by reducing with hydrogen. The presented results are important for unraveling different elements of heterogeneity and their effect on the performance of real polycrystalline catalysts. It is shown that a correlation can exist between the particle-support epitaxy and redox-cycling-induced shape changes.

Keywords

catalysis, redox-cycling, nanoparticle ensemble, epitaxy, faceting, shape changes, *in situ* X-ray diffraction

Metal nanoparticles on oxide supports are common catalysts for a variety of heterogeneous catalytic processes, including CO oxidation, NO_X reduction, methane combustion and hydrogenation for fuels.[1,2] Catalysts often consist of 4d noble metals, such as palladium (Pd).[3–8] Thorough understanding of how chemical processes take place on different nanoparticle (NP) facets and how its size and shape influence the catalytic activity will give chemical engineers information for the rational design of catalyst particles to improve their yield and lifetime. The detailed understanding of catalytic reactions in which NPs are involved is obscured by the morphology and surface structure of their ensemble.[9,10] Real catalyst systems are usually composed of randomly oriented metal or oxide NPs with a considerable size and shape distribution and both supported by oxide powders. This makes it difficult to isolate and investigate physical and chemical processes on NPs with a specific size, shape and orientation.[11,12] Even more complicated is the understanding of the role of metal-support interaction, which controls the overall energetics and sintering kinetics.[13,14] Model systems of NPs with a well defined orientation on a single crystal substrate enable the use of single crystal-like X-ray diffraction (XRD) to investigate physical and chemical processes occurring on a nanoscopic and atomistic level.[15] For example it has been demonstrated with *in situ* X-ray scattering techniques that the shape of the nanoparticles changes in reactive environments during a catalytic process.[16–22]

Equilibrium NP shapes are commonly determined from the Wulff construction where the surface energy of the particle is minimized by forming particular crystal facets.[23,24] Previous experiments have shown that Pd NPs, larger than approx 2 nm,[25] are predominately (100) and (111) faceted in the shape of a truncated octahedron.[17,26–30] Redox cycling plays an important role in oxidation catalysis[2] and as a processing step in tailoring the particle-support interaction.[31] In oxidizing environments, oxygen atoms in the gas phase adsorb on to the exposed surfaces of the metal NPs forming chemisorbed phases or thin surface oxides. This was investigated theoretically and experimentally.[32,33] Mittendorfer *et al.* performed *ab initio* simulations on how particles with low index (100), (111) and (110) facets react

with oxygen forming higher order facets like (112), (331) and (113). These facets become thermodynamically stable in higher oxygen chemical potentials.[32] Nolte *et al.* showed this experimentally, upon oxidation (112) facets are formed on the edges between (111) and (100) facets on truncated octahedral shaped Pd NPs.[33] Additionally, oxidation experiments were performed on single crystal and vicinal surfaces.[34,35] Work on these larger single crystals' surfaces forms a basis for the understanding of what could occur on the individual NP facets. Past experiments demonstrated that high index facets rearrange into other high index facets upon oxygen adsorption. For example Westerström *et al.* showed that (553) facets rearrange to (332) and (111) facets[34] and Vlad *et al.* showed that (112) facets rearrange into (113) and (335).[35]

In this work the reversible response of a Pd NP ensemble upon redox cycling, between clean UHV and mild oxidizing conditions, was investigated with surface sensitive XRD. The high angular resolution, which is not easily achievable with other techniques, allowed to uncover that the NP ensemble mainly consists of two types of particles. These have similar shapes but distinctly different epitaxial relationships as also manifested by different interfacial lattice registries. Both types of particles are found to change their shape differently upon oxidation, which implies that the metal-support epitaxy and resulting strain can have a decisive influence on the catalytic behavior of NPs. In addition to the NP dimensions and shape, we show that considerable surface stress and strain develops upon oxidation and reduction, as deduced from the asymmetry in the facet scattering signal around the Pd Bragg reflections.

Results and Discussion

Nanoparticle Ensemble Morphology

The *in situ* experiments were performed at the P23 *in situ* and nano X-ray diffraction beamline of PETRA III at Deutsches Elektronen-Synchrotron (DESY) with a portable ultrahigh

vacuum (UHV) sample environment allowing for controlled oxidation.[36] The Pd nanoparticles were deposited on a single crystal MgO(001) substrate with molecular beam epitaxy (MBE). The sample was exposed to air while transferring into the *in situ* sample environment. Therefore, several cycles of cleaning were performed to remove surface oxides. This consisted of oxidation in approximately 1×10^{-4} mbar O_2 pressure and subsequent reduction by heating to 973 K in UHV after the oxygen was pumped out of the chamber. The cleaning cycles were performed until changes in the X-ray scattering signal were observed upon oxidation and reduction, which indicated that the NPs' shapes were responding to the oxygen exposure. The following data presented in this section were collected on cleaned Pd NPs at 710 K in a UHV pressure of 6×10^{-9} mbar, at a chemical potential below the formation of surface oxides.[37]

Epitaxial NPs deposited with MBE on atomically smooth single crystal supports typically exhibit an angular distribution of 1° to 3° around the surface normal. In order to characterize the in-plane mosaic spread of the Pd NP ensemble, a rocking scan around the surface normal, ω, of the Pd 111 Bragg peak was performed. This is shown in Figure 1(a). The main central peak arises from Pd NPs with a cube-on-cube relation with respect to the MgO support, *i.e.* the main crystal axes of NP and MgO are aligned, in agreement with previous results concerning the epitaxy Nolte *et al.*.[33] As can be seen in Fig. 1(a), the mosaicity of the sample is not a single component but it has two prominent features at ±3.7° on either side of the main peak. The shoulder peaks are indicative of an epitaxially favorable orientation; a significant proportion of particles in the ensemble have a ±3.7° rotation in-plane with respect to the cubic MgO lattice sites. The cube-on-cube oriented NPs will be denoted as Pd[CoC] and the rotated NPs as Pd[R±3.7]. By comparing the intensity of the central peak with the shoulders, it is estimated that the Pd[R±3.7] particles make up approximately 1% of the NP ensemble. Both epitaxies result in coincidence lattices at the interface, as illustrated in Supplementary Information Figure S1. The Pd[CoC] epitaxy leads to 14×14 Pd unit cells on 13×13 MgO unit cells, while the ±3.7° rotation of the Pd lattice results

in a coincidence of 8×8 Pd unit cells on 7×7 MgO unit cells. Using the lattice constants of 3.89 Å and 4.21 Å for Pd and MgO, respectively, leads to a tensile interfacial strain of 0.5% for the Pd[CoC] particles and 5% compressive strain for the $\pm 3.7°$ Pd[R$\pm$3.7] ones. From the positions of the Bragg peaks, which are found to not deviate significantly from those expected for bulk Pd, it is concluded that the interfacial strain state is quickly relaxed within the particles. Considering geometrical arguments, like the fact that the bottom facet of the particles consists of a nearly square (001) facet, it follows that the bonding at the triple phase boundaries of the two types of particles must be different.

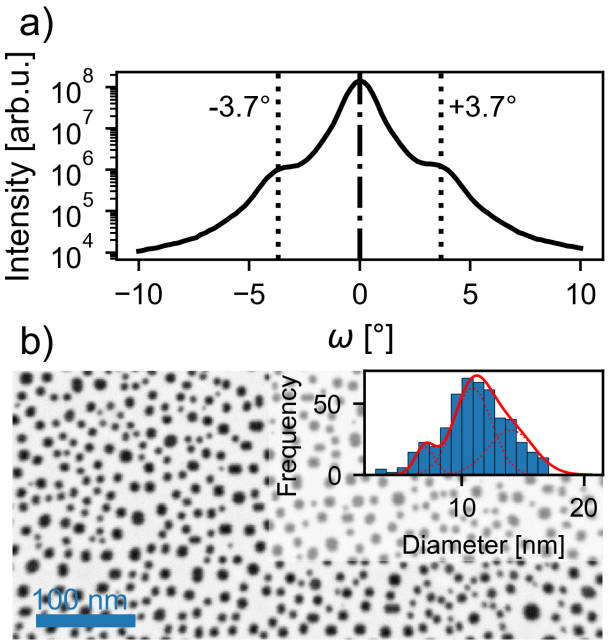

Figure 1: (a) Sample rotation, ω, rocking scan around the Pd 111 reflex for the NP mosaicity. The Pd 111 reflex is located at $\omega = 0$, the two shoulders are indicative of coherent scattering of particles which are rotated by a fixed amount in-plane, $\omega = \pm 3.7°$ as indicated by the dotted line, from the expected cube-on-cube [001] epitaxy on MgO. (b) SEM micrograph of the Pd NPs, inset, histogram of the particle size distribution consisting of three Gaussian components. Red lines shows the fitted distribution with three components shown as the dotted red lines.

The average diameter of the Pd[CoC] and Pd[R$\pm$3.7] NP ensembles was determined from post experiment *ex situ* scanning electron microscopy imaging. Figure 1(b) is a SEM image of the Pd NPs. The particle size distribution can be well described by three Guassians with

average diameters of 6.9 ± 0.3, 10.7 ± 0.8 and 13.8 ± 2.3 nm. The particle coverage estimated from the SEM image was around 22 %. Observation of the NP diameter heterogeneity is readily seen in the SEM imaging.

While SEM indicates three NP sizes, X-ray scattering patterns around the Pd 111 reflex only reveal two distinct types of particles. The morphology of these two types of particles was examined by analysis of the X-ray line scans across the Pd 111 reflex in different directions. The coordinate system in the X-ray line scans are in reciprocal lattice vectors, units of reduced lattice units [r.l.u.] relative to the dominant Pd[CoC] epitaxy unit cell with a lattice constant of 3.89 Å. The height and diameter of the two types of NPs were determined by the Pd 111 diffraction peak's full width at half maximum (FWHM). The average diameter of the Pd[CoC] particles yielded 14.2 ± 0.3 nm and the height 9.3 ± 0.2 nm. The average diameter of Pd[R±3.7] particles was determined to be 16.8 ± 0.1 nm and the height to be 8.2 ± 0.4 nm. The X-ray diffraction patterns used to determined these particle dimensions are shown in the Supplementary Information Figure S2.

The discrepancy between the observed distribution particle sizes in the SEM imaging compared to the particle diameters of the two types of particles determined from XRD can be understood by considering the following. Microscopy techniques give an area average while diffraction techniques render a volume average, which results in a systematic shift to larger values. Additionally, shadowing of the nanoparticles in the SEM image can also contribute to the size discrepancy. While two distinct types of particles were observed in the X-ray scattering patterns, three distributions are observed in the SEM imaging. One to one assignment can not be made between the epitaxial relations of the Pd[CoC] and Pd[R±3.7] particles to the different size distributions observed in the SEM image. It is likely the NPs in the diameter 10 - 15 nm range can have either Pd[CoC] or Pd[R±3.7] epitaxy. The small number of 6.9 nm diameter particles seen in the SEM was not observed as a different type of particle in the X-ray scattering but rather they are likely to be similar to and averaged out with the Pd[CoC] particles, as observed in previous studies, similar sized NPs have a

Pd[CoC] epitaxy.[16,33] High resolution XRD is able to separate the Pd[CoC] and Pd[R±3.7] particles in angular space, allowing the particle dimensions of the different epitaxy types of particles to be determined, which is otherwise indistinguishable with microscopy techniques.

Under equilibrium conditions with O_2 partial pressure $< 1 \times 10^{-8}$ mbar at 700 K Mittendorfer *et al.* calculated that (112), (113) and (331) facets are stable on Pd NPs at this O_2 adsorption chemical potential.[32] By utilizing the NP dimensions determined from XRD, the stability of different facets and minimizing surface energies, the theoretical shapes of the Pd NP were postulated. Figure 2 shows several views of atomistic sketches of the proposed NP shape and faceting of the Pd[CoC] particles (blue) and the larger Pd[R±3.7] particles (green) from the measured NP dimensions under equilibrium conditions. The particle is expected to be truncated predominately by (100), (111) facets along with (112), (113) and (331) facets along the edges of the (100) and (111) facets.

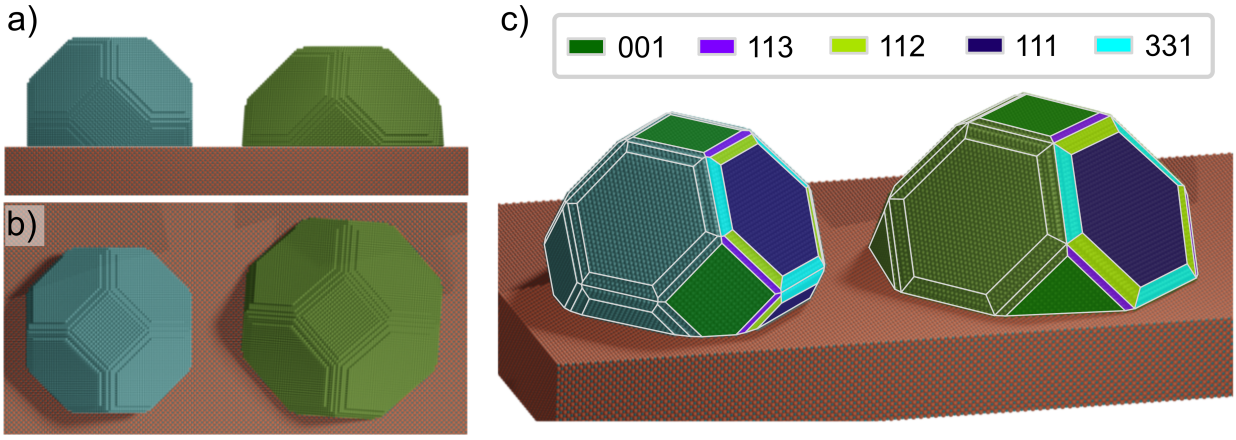

Figure 2: Atomistic 3D sketches of the postulated NP shapes from XRD determined particle dimensions in different angles, (a) from the side and (b) top view. The different facets of the NPs are highlighted in (c). The cube-on-cube epitaxial particles (blue) and ±3.7° rotated particles (green) on a MgO(001) substrate are illustrated. The cube-on-cube particles are slightly taller while the ±3.7° rotated particles have a larger diameter. The degree of truncation of the ±3.7° rotated particles is larger with an height to diameter aspect ratio of 0.49 compared to the cube-on-cube particles' aspect ratio of 0.66.

The degree of truncation of the NP on the particle-substrate interface is used to estimate the adhesion energy for truncated octahedral shaped particles, given by $E_{ads} = \gamma_{100} \cdot \frac{N_T - N_B}{N_T}$ from the Wulff–Kaichew construction.[38] Here, γ_{100} represents the surface energy of the (100)

facets, $\gamma_{100} = 1.51$ J/m^2.[39] N_T and N_B are parameters denoting the number of atomic layers on the top and bottom part of the particle. The difference between N_T and N_B describes the degree of truncation. The adhesion energy was determined to be $E_{ads} \approx 1.03$ J/m^2 for the Pd[CoC] particles, higher than reported values in past experiments and theory, in the range from 0.5 to 0.9 J/m^2.[26,33,40] The adhesion energy for the Pd[R±3.7] particles was determined to be $E_{ads} \approx 1.54$ J/m^2. The degree of truncation of the bottom part of the Pd[R±3.7] particles is large, these particles are likely truncated pyramid shaped rather than truncated octahedral.[41] The larger adhesion energy and higher degree of truncation of the Pd[R±3.7] particles compared to the Pd[CoC] particles is explained by the smaller number of unit cells in the coincidence superlattice of the Pd-MgO interface. The Pd-MgO interface of the smaller Pd[CoC] particles contains a higher density of dislocation defects from the lattice mismatch leading to the truncated octahedral shape.[41,42]

Nanoparticle Shape and Faceting

The faceting and shape of the nanoparticles were investigated in detail by analyzing the X-ray diffraction signal around the Pd 111 Bragg peak. Figure 3(a) shows an example of a model truncated-octahedral-shaped NP from the Wulff construction for particle shape on a substrate.[24,28] This idealized model particle shape has only (001) and (111) facets to illustrate the location and direction of the diffracted signal from the facets in reciprocal space. The corresponding diffraction pattern in the $[\pm\Delta\mathrm{H}, \mp\Delta\mathrm{K}, \Delta\mathrm{L}]$ reciprocal plane centered around the (111) reflex is depicted above. The directions of the facet scattering streaks are used to determine the facets present on the NPs. These signals emanate in directions perpendicular to the facets' surface planes, analogous to crystal truncation rods from surfaces.[16,33] To a good approximation, the integrated intensity of the facet scattering close to the Bragg reflex is proportional to their area. The area of the facets is not easily quantified due to the low scattering signal and disentangling the background signals from the Bragg reflex and nanoparticle mosaicity. However, the relative change in intensity can be used to infer

relative change in the facet area. The particle depicted in Figure 3(a) consists of (001) and (111) facets, scattered signal from the (001) facets are along the [11L] direction indicated by the dark green arrow and lines. The (111) facets are indicated by the dark blue arrow and corresponding lines above.

First, we will discuss results from the clean Pd NPs. The location of the scattering from different facets was observed in reciprocal space on the $[\pm\Delta H, \mp\Delta K, \Delta L]$ plane, denoted as $[H, K = 2 - H, L]$ in absolute r.l.u. around the 111 reflex of the Pd[CoC] NPs as sketched in Figure 3(b)I. The location of scattering signal of different facets are represented by the straight lines intercepting the 111 Bragg peak in different directions. The 111 reflexes of Pd[R±3.7] particles are located at (H=0.92, K=1.08) and (H=1.08, K=0.92) denoted by 111_R. While these particles are also expected to be faceted, the intensity of their side facet signal is on the order of 100 times weaker and was not observed over the background of scattering from the Pd[CoC] particles. The only information on the Pd[R±3.7] particles' faceting is from the scattering along the (11L) CTRs which contains information of the (001) facets, shown as the green dashed line labeled $(001)_R$. The circular lines represents the positions of isotropic Debye-Scherrer scattering arising from the {111} and {200} lattice planes of randomly oriented particles. Panels II and III of Figure 3(b) are the X-ray line scans in the reciprocal space map in order to investigate the NP shape and faceting, indicated as the dashed and dotted lines in Figure 3(b)I.

The line scans at L = 0.65, 0.75 and 0.85 are shown in panel III of Figure 3(b), their location in reciprocal space is indicated with the dotted lines of the same color in (b)I. Open circles represent the acquired data and the red lines are the fitted multiple pseudo-Voigt models. The scattering direction of the particles' (001) top facets are in the L direction and corresponds to the (11L) CTR. The (11L) CTR of the Pd[CoC] particles in the center dominates the line scans at (H = 1, K = 1) while the (11L) CTRs and signal from $(001)_R$ facets of Pd[R±3.7] particles are located at (H = 0.92, K = 1.08) and (H = 1.08, K = 0.92), indicated by the green arrow in Figure 3(b)III.

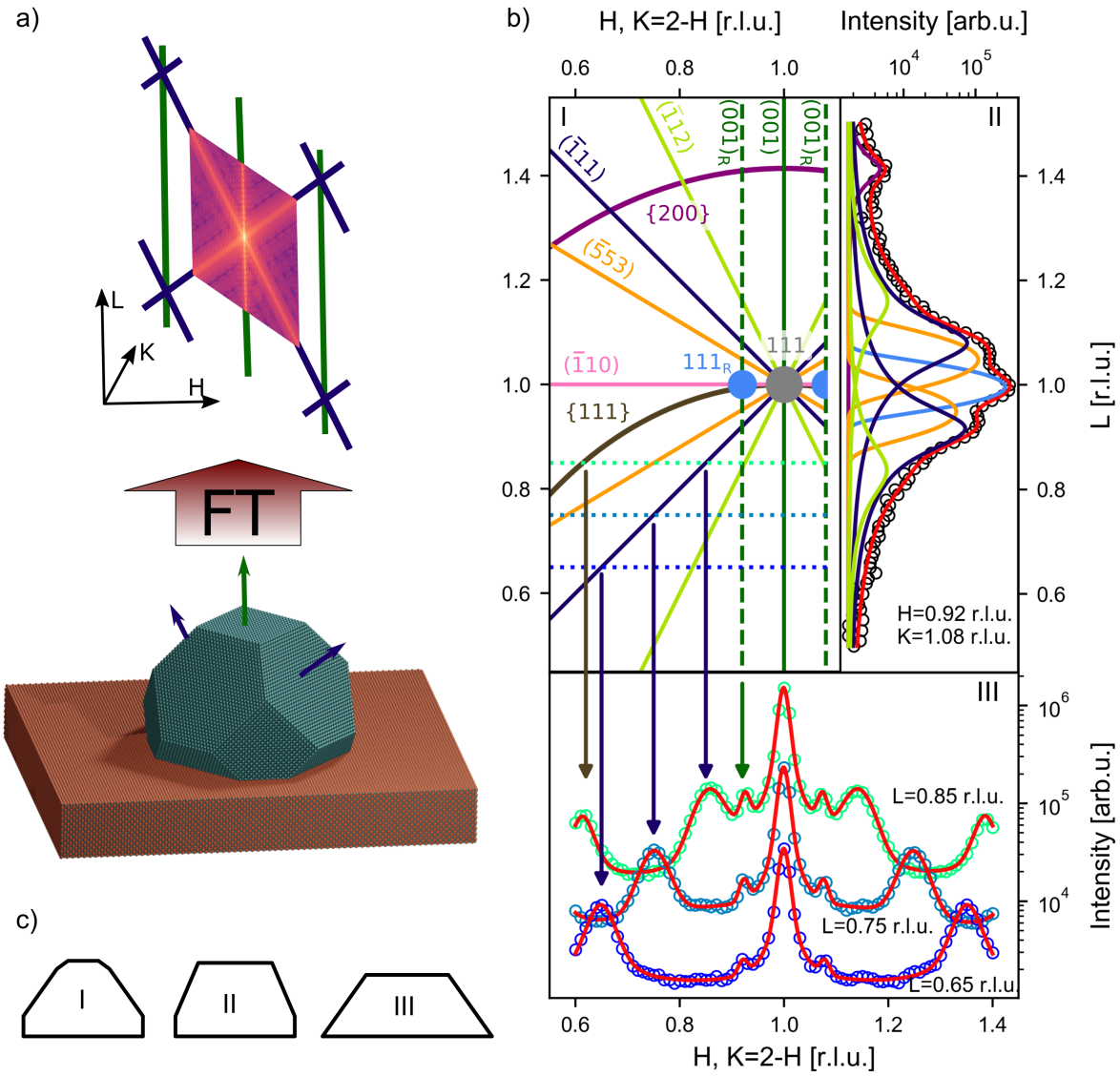

Figure 3: (a) bottom, sketch of model truncated octahedral Pd NP on a substrate and above, the corresponding simulated diffraction pattern expected around the Pd 111 reflex. The (001) and (111) facets are indicated with the green and blue arrows respectively. (b)I Reciprocal space map of the $[\pm\Delta H, \mp\Delta K, \Delta L]$ plane around the Pd 111 reflex. Locations of scattering observed in the experiment are illustrated on the map; the Pd 111 reflexes (dots), facets (straight lines) and Debye-Scherrer scattering (curved lines). The dotted and dashed lines shows where in reciprocal space the corresponding data shown in panels II and III were acquired. (b)II shows the [L] scattering pattern along $[H = 0.92, K = 1.08]$, circles are the data points and red line is the fitted model, with components in solid color lines corresponding to the colors in (b)I. (b)III shows three line scans along $[H, K = 2 - H]$ at L = 0.85, 0.75 and 0.65. The circles are the data points and reds line are the fitted models. Arrows indicate peak assignment according to (b)I. (c) depicts particle cross sections showing possible faceting for the Pd[CoC] particles; (c)I consisting of (001), (111) and (112) facets or (c)II consisting of (001) and (553) facets. (c)III depicts Pd[R±3.7] particles with smaller aspect ratio, primarily consisting of (111) side facets.

Scattering arising from the (111) facets is evident in these line scans, located along [$\Delta H = -\Delta K = \Delta L$] in this plane, as indicated by the dark blue arrows in Figure 3(b). Between the scattering signal of the (11L) CTR and (111) facets there is broad scattering arising from (112) facets of Pd[CoC] particles overlapping with the Pd[R±3.7] particles (11L) CTR for L values closer to 1. This signal cannot be neglected for the scattering data to be fitted satisfactorily. Signal from (553) facets should also be observable in this direction, however it becomes weaker the further away in $[\Delta H, -\Delta K]$ from the 111 peak. Therefore, line scans along L at (H = 0.92, K = 1.08) were used to investigate the (553) facets.

Shown in Figure 3(b) Panel II is a L line scan at (H = 0.92, K = 1.08). This line scan coincides with the (11L) CTR across the 111_R Bragg peak of the Pd[R±3.7] particles. The different components fitted to the data are the solid color coded lines corresponding to the various scattering signals in this plane as shown in Figure 3(b)I. The peak observed at L = 1.4 arises from the tail of the Pd 002 peak of [110] oriented particles, in which a small minority are present, elongated particles in the SEM image Figure 1(b) and see Supporting Information. In addition to the 111_R Bragg peak of the Pd[R±3.7] particles, the shoulders at higher and lower L consist of three components associated with the (111), (112) and (553) faceting of the Pd[CoC] nanoparticles. From these line scans we conclude that in addition to the expected (111) and (001) facets from the Wulff construction of a model truncated octahedral particle, the clean particles exhibit other facets, namely (112) and (553) facets, which were observed in the scattering patterns and are also depicted in Figure 3(b)I. The existence of all these facets cannot occur on one particle, rather the Pd[CoC] particles in the ensemble is made up of particles having either (111) and (112) facets or (553) facets, see Figure 3(c).

The asymmetry observed in the structure factor between larger and smaller momentum transfer around the Bragg reflex is an indication of strain in the outer atomic layers of the nanoparticles.[43,44] For small compressive strain, the structure factor is larger at momentum transfers above the Bragg peak compared to below. This phenomena is further illustrated

in the Supporting Information, Figure S5. The higher intensity observed for momentum transfers L > 1 in Figure 3(b)II indicates that the facets of the clean NPs experience a compressive strain and this is more pronounced for the (553) facets as compared to the (111) facets.

The (110) facets are not observable in the [H, K = 2 − H, L] plane. Therefore to investigate the presence of (110) facets, a 2D reciprocal space map was acquired in the [H, K, L = 1] plane, this is shown in Figure 6(a) in the latter section. The scattering signals from the (100) and (110) side facets were observed around the Pd(111) reflex in this map. In UHV conditions at 700 K Mittendorfer *et al.* predicted the presence of (112) and (331) facets.[32] In our experiments in UHV conditions consisting of 6×10^{-9} mbar of residue gases at 710 K, (331) facets were not distinctly observed in the scattering signal but rather (110) facets were observed. However, Mittendorfer *et al.* notes the energy difference for stability is so small for the (331) and (110) facets and one cannot with certainty predict (110) facets are unstable, thus these experimental results remain consistent with theory.

In order to describe the shape of the Pd[CoC] particles, the presence of facets determined from the aforementioned X-ray scattering data in combination with the particle height and diameter was used to construct possible projected shapes as shown in Figure 3(c). The combination of the scattering patterns along [H, K = 2 − H], [L] and in-plane [H, K, L = 1] around the Pd(111) reflex provides information on the faceting between the (001) and (110) facets. The surface plane connecting the (001) and (110) facets can either be combination of (111) and (112) facets as predicted by Mittendorfer *et al.*[32] (Figure 3(c)I) or by (553) facets (Figure 3(c)II). Steeper (553) facets were also detected in the X-ray scattering patterns which are constructed of monolayer (111) faceted steps for every five atoms wide on (111) terraces.[34] The NPs studied in this work are a heterogeneous ensemble and it is expected to be a combination of the two aforementioned extremes rather than one or the other. We assume the Pd[R±3.7] particles are shaped as predicted with the Wulff construction and in past experimental studies making up of primarily (111) facets on the sides as sketched in

Figure 3(c)III.[17,28,33,41] The higher aspect ratios of the Pd[CoC] particles of 0.64 makes it energetically more favorable for steeper (110) or (553) facets to form. While the Pd[R±3.7] particles have a relative lower aspect ratios of 0.50 it is energetically more favorable to form (111) facets.

Nanoparticle Oxidation and Reduction

The following section covers the response of the Pd NPs to different oxidation and reduction conditions. It was investigated upon exposure to O_2 at two different pressures, 1×10^{-4} and 5×10^{-3} mbar. The reversibility of changes in the NPs dimensions and facets upon reduction was investigated by pumping out the O_2 and subsequent heating for a reducing environment under UHV. Reduction of the nanoparticles was also investigated by introducing H_2 after removing the O_2 out of the chamber. The oxidation-reduction experiments consisted of obtaining X-ray scattering patterns as described in the preceding sections, with the temperature maintained at 710 K during data acquisition. Initially in an UHV pressure of $< 5 \times 10^{-9}$ mbar, afterwards, subsequent leaking of O_2 into the chamber. Afterwards the O_2 was pumped out of the chamber and the sample was annealed at 973 K for 30 minutes to reduce the NPs. A set of X-ray scattering data was obtained after returning to 710 K. Then 1×10^{-4} mbar of O_2 was introduced to the sample environment and the final step consisted of pumping out the O_2 and introducing 1×10^{-5} mbar of H_2.

Table 1: Sequence of nanoparticle dimensions in diameter, d, height, h and their ratio in different oxidizing and reducing environments determined from the FWHM across their Bragg peaks.

Introduced gas	Pd[CoC] particles			Pd[R±3.7] particles		
pressure [mbar]	d [nm]	h [nm]	Ratio	d [nm]	h [nm]	Ratio
0	14.2 ± 0.03	9.3 ± 0.02	0.66	16.8 ± 0.11	8.2 ± 0.43	0.49
$p_{O_2} = 1 \times 10^{-4}$	14.0 ± 0.03	–	–	16.2 ± 0.15	8.1 ± 0.13	0.5
$p_{O_2} = 5 \times 10^{-3}$	13.5 ± 0.03	–	–	15.9 ± 0.1	8.1 ± 0.2	0.51
0	14.7 ± 0.03	9.4 ± 0.03	0.64	16.7 ± 0.16	8.2 ± 0.24	0.49
$p_{O_2} = 1 \times 10^{-4}$	13.9 ± 0.02	8.9 ± 0.03	0.64	15.9 ± 0.15	8.0 ± 0.2	0.51
$p_{H_2} = 1 \times 10^{-4}$	14.4 ± 0.03	9.3 ± 0.02	0.65	16.5 ± 0.12	7.8 ± 1.16	0.47

Observation of the the peak width broadening elucidates changes in the nanoparticle dimensions upon oxidation and reduction. Table 1 summarizes the dimensions of the Pd[CoC] and Pd[R±3.7] NPs obtained from the Bragg peak FWHM in the oxidation-reduction environments explored. As it is shown in Table 1, under oxidizing conditions, 1×10^{-4} mbar of O_2 the particles' dimension decrease both in diameter and height for two types of particle epitaxy in the ensemble and decreases further in higher O_2 pressure of 5×10^{-3} mbar. Upon reduction by annealing in UHV or in H_2 the particle dimensions recover.

Upon oxidation a surface oxide layer may form on the particles. These can have different super cells, like $(\sqrt{5} \times \sqrt{5})$R27° on (100) facets and $(\sqrt{6} \times \sqrt{6})$ on (111) facets.[28,45–47] These surface oxide phases reduce the number of metallic lattice planes and hence broaden the Bragg peak in the corresponding direction, yielding smaller apparent particle dimensions. The Pd[R±3.7] particles show greater change in their diameter relative to their height during the oxidation-reduction cycle. In contrast, for the Pd[CoC] particles the proportional change in their diameter and height is similar. The response of the Pd[R±3.7] is different from the observation made by Kasper *et al.*, where the particles became flatter initially then reduced in size laterally in this O_2 pressure range.[28] This can be explained because the Pd[R±3.7] particles here were already initially flatter in UHV conditions, yielding a larger change in their diameter compared to their height.

Figure 4 shows the evolution of the line scans in the $[H, K = 2 - H]$ direction at $L = 0.85$ in different atmospheres. The corresponding plots at $L = 0.75$ and 0.65 can be found in the Supporting Information, Figure S6. The response of the (001), (111), (112) and (553) facets of the Pd[CoC] particles, and the (001) facets of the Pd[R±3.7] particles upon oxidation and reduction were observed in this region of reciprocal space. Figure 4(a) shows the line scans for the different gas conditions while Figure 4(b) shows the difference in the scattering intensities between treatment steps. The most prominent change observed here is the substantial reduction of the Pd[R±3.7](11L) CTR located at $[\pm\Delta H, \mp\Delta K] = \pm 0.08$ [r.l.u.] upon introduction of 1×10^{-4} mbar of O_2. The signal decreased further when the

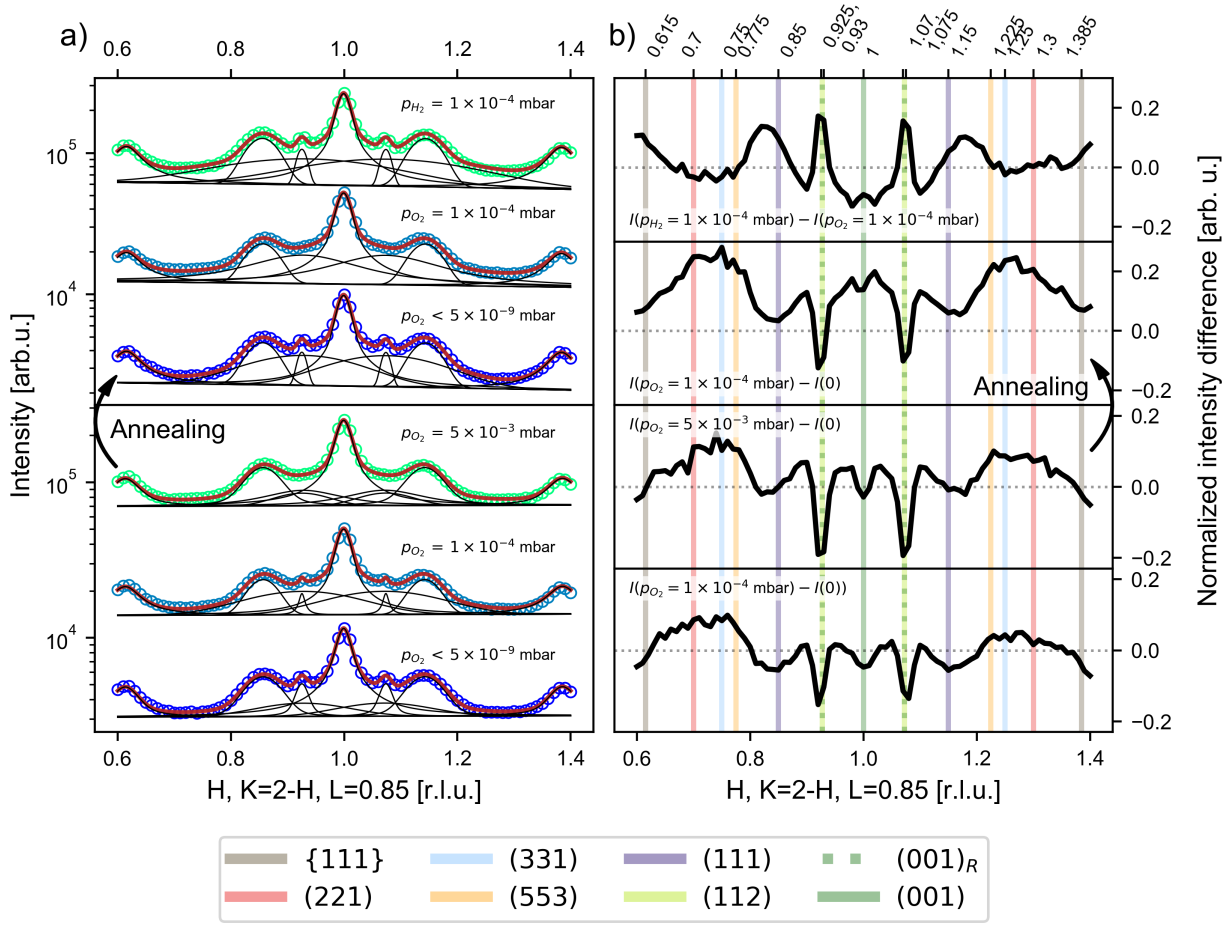

Figure 4: (a) Evolution of X-ray scattering patterns in different sample environments in the $[\mathrm{H}, \mathrm{K} = 2 - \mathrm{H}]$ direction at $\mathrm{L} = 0.85$. Circles are the data points, red lines are the fitted model, and black lines are the individual pseudo-Voigt components of the fitted model. The data was acquired sequentially from bottom to top. The fitted parameters can be found in the the Supporting Information, Table S1. (b) are the sum normalized difference in scattered intensity between the various steps in the experiment. Vertical colored lines and dots depict where signal from the corresponding facets is expected.

O_2 pressure was raised to 5×10^{-3} mbar. Averaging the fitted intensities over the different experiments and oxygen pressures (see table S1 for the numerical values) results in a significant loss of approximately 50-70 %, of the (001) facet signal. Upon reduction by annealing or introduction of H_2, the sharp peak recovers. This response of the Pd[R±3.7](11L) CTR is directly related to the (001) top facets becoming smaller upon oxidation, leading to rounder particles, possibly with (112) facets forming as previously reported by Nolte *et al.*.[33] The exact shape under oxygen, however, cannot be determined, because the signal of higher order facets of the Pd[R±3.7] particles is too weak and in the background of the signal from Pd[CoC] particles to be reliably distinguished. The response of the Pd[R±3.7](11L) rod is similar to what was observed in the previous work of Nolte *et al.* and it can be postulated that they form (112) facets on the edges between (100) and (111) type facets.[33]

For the Pd[CoC] particles, a slight decrease of the (001) facet signal was also observed but the change is not as significant (approx. 0-10 %, see table S1 for the numerical values). In contrast to the work by Nolte *et al.*, no appreciable increase in the scattering signal associated with the (112) facets was observed. However, the region of scattering from (112) facets is expected to be broad and overlaps with the Pd[R±3.7](11L) rod, which cannot be easily disentangled. The reduction and formation of facets during the oxidation-reduction steps can be identified in the intensity difference between the steps plotted in Figure 4(b). Rather than forming (112) facets upon oxidation, the increase in scattering further away from the Bragg peak suggests higher order facet formation such as (331) and (221) accompanied by a reduction of the (001) and (111) facet area. This result is consistent with theoretical studies. Mittendorfer *et al.* predicted the formation of (331) facets upon oxygen adsorption and Westerström *et al.* also showed that (553) surfaces rearrange to (332) facets, a closely indexed facet. The increased X-ray scattering at locations associated with these higher order facets indicate that during the oxidation process the particles becoming more rounded. The top most panel of Figure 4(b) shows the intensity differences between an oxidation step and subsequent reduction in H_2, the symmetry in the relative changes in scattering intensity

between the oxidation and reduction steps demonstrates the reversibility of the NP shape changes in oxidizing and reducing conditions.

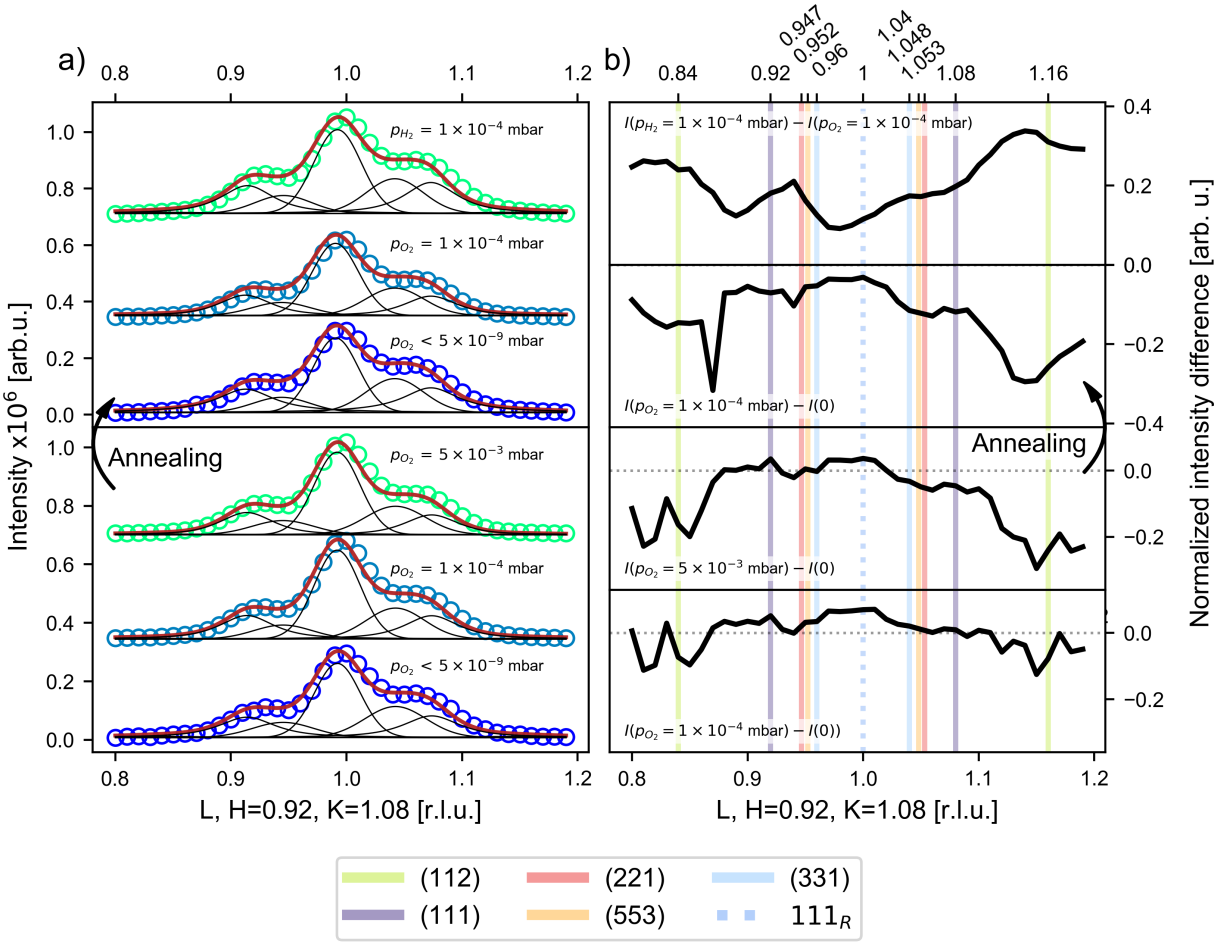

Figure 5: (a) Evolution of X-ray scattering patterns in different sample environments along the [L] direction at (H = 0.92, K = 1.08). Circles are the data points, red lines are the fitted model, and black lines are the individual pseudo-Voigt components of the fitted model. The data was acquired sequentially from bottom to top. The fitted parameters can be found in the Supporting Information, Table S2. (b) are the difference in scattered intensity between the various steps in the experiment. Vertical colored lines depict where signals from the corresponding facets occur.

More information about the facetting process is obtained from L scans. Figure 5 shows the X-ray line scans along $[0.92, 1.08, \mathrm{L}]$. Along this line in reciprocal space the Pd[R±3.7](11L) CTR is superimposed with contributions from different facet signal of the Pd[CoC] particles. The signal from the Pd[R±3.7](11L) CTR is several orders of magnitude smaller and the

changes in the signal observed here are primarily from the facets of the Pd[CoC] particles. Similar to the scattering patterns in the $[H, K = 2 - H]$ direction, the scattered intensity associated with the (112) facets decreases upon oxidation as shown in the intensity differences under different gas conditions, Figure 5(b). A similar behavior is observed during the oxidation of Pd(112) single crystal surface.[35] Also correlating with the change in scattering intensity in the $[H, K = 2 - H]$ direction, the (331), (221) and (553) facets scattering intensity does not decrease significantly. The scattering signals from these facets are located close together near the central Pd[R±3.7] 111 peak, thus are difficult to disentangle with their finite peak width. While not clearly evident in the intensity difference, the fitted pseudo-Voigt component associated with the (111) facets show a decrease in intensity upon oxidation in agreement with changes observed in the $[H, K = 2 - H]$ direction, fitted parameters are available in the Supporting Information, Table S2.

The distinctive difference in the scattering data observed between the Pd[R±3.7] and Pd[CoC] particles, is the different response of (001) facets in an oxidizing environment. In Figure 4 it is shown that the reduction of the top (001) facets of the Pd[R±3.7] particles is significantly more pronounced compared to the Pd[CoC] particles. This is an indication that the mass transport on the Pd[R±3.7] particles is enhanced compared to the Pd[CoC] particles. Thus the Pd[R±3.7] particles are able to form high index facets more readily.

Qualitative observation of the asymmetric changes in intensity with respect to the Pd Bragg peak along L shows the nanoparticles experience a tensile strain during oxidation and relaxes back to initial conditions when reduced. This is observed with the greater reduction in intensity at higher L, indicating the lattice spacing of the (001) facets increases, becoming more substantial at 5×10^{-3} mbar of O_2. Removal of the oxygen atoms with reduction of the nanoparticles shows the asymmetrical relaxation back inwards of the top layers with larger change in intensity at higher L.

In-plane [H,K] meshes were measured at L = 1 around the Pd 111 reflex, under UHV conditions and also in 1×10^{-4} mbar of O_2. The meshes were used to observe the changes

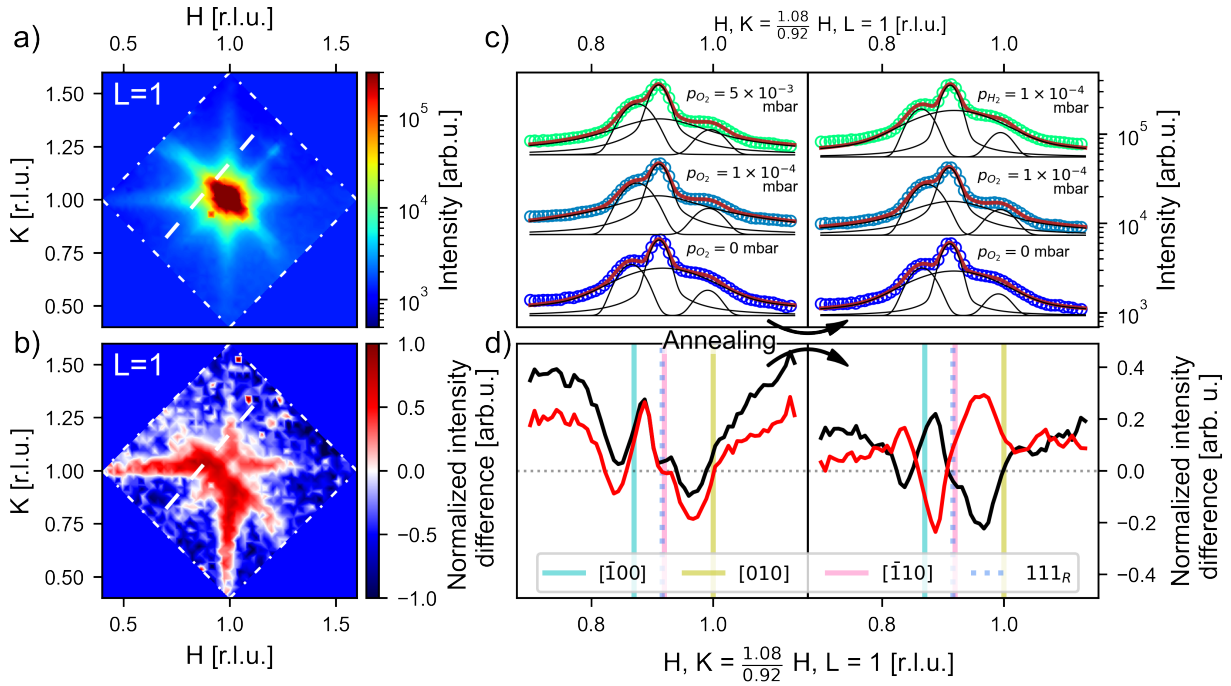

Figure 6: (a) X-ray scattering map of the [H,K] plane at L = 1, obtained in UHV conditions. Dot-dashed lines indicate the boundary of where the X-ray scattering map was obtained. The dashed line shows the location of the radial [H,K] X-ray scattering patterns across the Pd[R±3.7] 111 reflex shown in (c). (b) shows the normalized scattering intensity difference on the [H,K] plane at L = 1 under O_2 *vs.* UHV conditions. (c), X-ray scattering patterns in the radial [H,K] direction at L = 1 across the Pd[R±3.7] 111 reflex in different gas conditions. Left, two oxidation steps and right, oxidation and reduction. Circles are the data points, the red lines are the fitted model, and black lines are the individual pseudo-Voigt components of the fitted model. The experiments were performed sequentially from bottom to top. The fitted parameters can be found in the the Supporting Information, Table S3. (d) are the corresponding difference in scattered intensity shown in (c), black line is the difference between 1×10^{-4} mbar and UHV conditions for both left and right panels. Red (left) shows the difference between 1×10^{-3} mbar and UHV. Red (right) shows the difference at 1×10^{-4} mbar of H_2 *vs.* 1×10^{-4} mbar of O_2. Vertical colored lines and dots depict where signal from the corresponding facets occur.

of the in-plane (100) and (110) facets of the Pd[CoC] particles. Figure 6(a) shows the mesh on the [H,K] plane at L = 1 of the sample in UHV conditions, (b) is the difference between the scattered intensity in 1×10^{-4} mbar of O_2 compared to UHV conditions. Figure 6(c) shows the radial X-ray line scans across the Pd[R±3.7] 111 reflex, as indicated by the dashed line in the [H,K] mesh in Figure 6(a). The scattering pattern predominately consists of four components, the 111 Bragg peak of the Pd[R±3.7] particles, and $(\bar{1}\,0\,0)$, $(0\,1\,0)$ and $(\bar{1}\,1\,0)$ facet signal of Pd[CoC] particles. The $(\bar{1}\,1\,0)$ component is broad, indicating the facets are very small, overlapping with the Pd[R±3.7] 111 peak and the $(\bar{1}\,0\,0)$, $(0\,1\,0)$ facets.

Under oxidation conditions, there is a decrease in the scattered signal associated with the $(\bar{1}\,1\,0)$ facets, as evident in the X-ray scattering patterns shown in Figure 6(c) (fitted peak profile parameters can be found in the Supplementary Information, Table S3). The sum normalized intensity differences shown in Figure 6(d) also shows this decrease. However, this decrease is not observed in the difference mesh shown in Figure 6(b) because the sampling of the data points was a factor three smaller and the different background levels of the meshes contribute to the concealment of the very broad $(\bar{1}\,1\,0)$ component. It is noted that the zero position in the scattering difference in the mesh and line scans are heavily dependent on small changes in the sample alignment and background. As the $(\bar{1}\,1\,0)$ facets are reduced in O_2, (331) facets form, which are observed in the line scans in different directions, Figures 4 and 5. The broad decrease in intensity attributed the $(\bar{1}\,1\,0)$ facets explains the apparent shift of the features in intensity differences to lower momentum transfer shown in 6(d) compared to facet signal locations depicted by the coloured vertical lines. The intensity differences presented Figure 6(d), left panel, shows reduced scattering from the in-plane (100) facets in O_2, indicating these facets become smaller as higher order Miller index facets are formed, rounding the particles in agreement with observations in the line scans in other directions.

A distinctive feature observed in Figure 6(b) is the relative change in intensity at higher compared to lower [H,K] with respect to the Pd 111 reflex. The greater degree of change at lower momentum transfer is an indication the spacing of the surface atomic layers of

the (100) facets increased in an oxygen atmosphere. The surface strain of the Pd[CoC] nanoparticle (100) facets is characterized by comparing the scattered intensities between the $(\bar{1}\,0\,0)$ and the $(0\,1\,0)$ facets along the dashed line in Figure 6(a). As observed in the line scans, Figure 6(c), in UHV the scattering from the $(\bar{1}\,0\,0)$ facet has higher intensity at lower momentum transfer compared to the $(0\,1\,0)$ facets, this indicates the surface atomic layers of the $(\bar{1}\,0\,0)$ and the $(0\,1\,0)$ facets type are under a tensile strain. This is in contrast to the (111) type facets observed in the scattering pattern along [0.92,1.08,L]. As O_2 is introduced to the system, the intensity difference associated with the $(\bar{1}\,0\,0)$ facets at lower Q is greater than that of the $(0\,1\,0)$ facets at higher Q. This is seen in Figure 6(b), where there is a larger intensity difference observed at momentum transfers below the Pd 111 reflex. The line scan differences, Figure 6(d) also show the same at locations indicated by the vertical colored bars. This indicate additional tensile strain in O_2 as a consequence of oxygen adsorbed onto the surface. The asymmetric behavior of the change in the intensity during the oxidation and reduction processes are similar for Pd[R±3.7] and Pd[CoC] type NPs in the ensemble. This includes the (001) facets of both types of particles, and the (111) and (001) facets of the Pd[CoC] particles. The increase in the spacing of the surface atomic layers during oxidation is attributed to the formation of a single surface oxide layer or chemisorbed oxygen entering the lattice.[35,47,48] The right panel of Figure 6(d) shows the recovery in intensity after the subsequent reduction step in H_2, showing that the change in in-plane surface strain and formation of new facets are also reversible.

The minimization of Gibbs free energy, explicitly including the adsorption of oxygen, is the driving force for the observed phenomena. Higher order facets such as the (112) facet contain an increased number of fourfold coordinated adsorption sites compared to threefold sites on the (111) surface.[33,35] With the formation of high index facets, the nanoparticles become rounder providing more adsorption sites on the nanoparticle surface for oxygen species to be adsorbed. Fourfold coordination sites for oxygen at high index facets are energetically more favorable.

Conclusion

In this work we report on the response of Pd nanoparticle facets upon oxidation and reduction in a heterogeneous ensemble. Pd nanoparticles with similar truncated octahedral shape but with different epitaxial relations were observed. The sample consisted of predominately a cube-on-cube Pd[100]//MgO[100] relation along with a smaller proportion (approx. 1%) of nanoparticles rotated $\pm 3.7^{\circ}$ around the surface normal from the cube-on-cube relationship. The Pd[R$\pm$3.7] particles within the ensemble show relatively more pronounced shape changes upon redox cycling, as observed *in situ* from changes in the X-ray scattering signals. It is concluded that the mass transport on the Pd[R$\pm$3.7] particles is enhanced compared to the Pd[CoC] particles, resulting in a large reduction of the top (001) facet and formation of other high index facets. The shape changes observed were completely reversible either by annealing or reducing in H_2.

This work also demonstrates the ability of using X-ray scattering *in situ* to observe the atomic surface strain of different facets on metal nanoparticle ensembles. The difference in the asymmetric scattered intensity from surface truncations between oxidation and reduction cycles was used to qualitatively infer relative changes of the surface strain experienced on the nanoparticle facets. We observed an increased surface tensile strain on the (001) facets in an oxidative environment which is relaxed again upon reduction.

The nanoparticle shape changes observed takes place at low O_2 pressures compared to real redox reactions in heterogeneous catalysts.[37,47,48] However, under real redox conditions the nanoparticles are exposed to a flow of a gas mixture and the reactions takes place continuously. In real catalytic systems with kinetics and mass transport taking place, the local oxygen coverage can be similar to our experimental conditions at low pressures.

In summary, we have shown a correlation between epitaxy and shape response upon oxidation in a heterogeneous ensemble of Pd nanoparticles on MgO(001) substrates. This implies that the exact metal-support interface structure plays a role for the facets being exposed under catalysis-relevant conditions. It remains unclear to what extent the strain

state and/or the triple phase boundaries, which differ for various epitaxial relationships, need to be taken into account. These results show how the interfacial bonding geometry and resulting epitaxy can play a role for metal particles' heterogeneity, shapes and sizes. Such information is important for disentangling and understanding the catalytic response of supported epitaxial metal nanoparticle ensembles.

Experimental Methods

Sample Preparation and Pre-Synchrotron Characterisation

The Pd nanoparticle samples were deposited on a MgO(001) substrate by means of electron beam evaporation in an UHV chamber, with a base pressure of 1×10^{-10} mbar. The MgO(001) substrate was prepared by cleaning in an ultrasonic bath of isopropanol and ethanol for 15 minutes each, then annealing in a tube furnace in air at 1273 K (1473 K/h ramp up and down) for 1 hour prior to introducing it to the UHV system. The substrate was degassed for 1 h at 770 K, followed by two cycles of Ar ion sputtering for one hour and annealing in oxygen. Ar ion sputtering was performed at room temperature with an argon partial pressure of 7×10^{-6} mbar and an ion energy of 1 keV (0.6 keV for the second cycle). The sample was annealed for one hour, at 770 K at an oxygen partial pressure of 1×10^{-5} mbar.

Prior to Pd evaporation, Auger electron spectra and low energy electron diffraction patterns were recorded to confirm the MgO surface termination and absence of contaminates, (see Figure S7 in Supporting Information). Directly following the surface preparation, the equivalent of 10.5 (001) monolayers of palladium was deposited over for 12 min at 500 K.

Sample Environment

After Pd deposition the sample was subsequently taken out of the UHV system and transferred into a portable *in situ* XRD UHV oxidation chamber. The *in situ* sample environment consists of a Be cylinder with a wall thickness of 2 mm, used as an X-ray window. The cham-

ber is pumped with a turbo pump and can achieve a base pressure of 5×10^{-10} mbar at room temperature. The chamber has a ceramic heater and a dosing valve is used to leak 99.999% purity O_2 into the chamber for control of the sample environment. As the sample and chamber was exposed to air during the transfer from the sample preparation system to the portable chamber, the system was baked at 110 °C to be able to achieve UHV conditions after introduction of the sample to the chamber.

PETRA III P23 *In Situ* X-ray Diffraction Experiments

The diffraction experiments were carried out at the beamline, P23 *in situ* and nano X-ray diffraction beamline of PETRA III at DESY. The X-ray beam had an energy of 12 keV and a beam size of 100 µm in the vertical and 500 µm in the horizontal. The experiment was performed in grazing incidence geometry with an incidence angle of 0.18°, close to the sample's critical angle. A LAMBDA 750K 2D pixel detector with a GaAs sensor was used. Line scans were acquired in the $[\pm\Delta H, \mp\Delta K, \Delta L]$ plane to avoid strong scattering from the MgO 111 substrate peak which is located nearby in the $[-\Delta H, -\Delta K]$ direction and overlaps with the scattering originating from the nanoparticle facets. Acquiring the scattering pattern along the $[\pm\Delta H, \mp\Delta K]$ direction is also advantageous because it enables the integration of the nanoparticles' in-plane mosaic spread where the diffraction condition is fulfilled for a range of rotated particles, providing better signal to background statistics of the particle facets.[49]

X-ray Scattering Data Processing

The features observed in the X-ray scattering data were fitted to pseudo-Voigt profiles using least-square minimization using the trust region method. The fitting regions were additionally weighted in respect to peak intensity and feature density. The X-ray scattering data acquired in UHV were fitted first and used as starting points for the the fitting of the scattering patterns in different gaseous environments. The facets' peak positions were constrained

to a region of ± 0.05 in reduced lattice units from their expected positions and the position of the symmetrically equivalent peaks were correlated by the same distance to the central peak. In the case of the scattering patterns in the $[\mathrm{H}, \mathrm{K} = 2 - \mathrm{H}]$ direction, amplitude of the symmetrically equivalent peaks were fitted to the same value.

The X-ray diffraction peak width is inversely proportional to the number of coherently scattering lattice planes in the direction of the scattering vector. The height and diameter of the nanoparticles were determined by the Pd 111 diffraction peak's full width at half maximum (FWHM), $D = 2\pi/\Delta Q$ in different directions. The particle dimensions were observed from the Pd[CoC] particles' Bragg peak FWHM in the $[+\Delta\mathrm{H}, -\Delta\mathrm{K}]$ direction and the $[+\Delta\mathrm{H}, +\Delta\mathrm{K}]$ direction for Pd[R$\pm$3.7] particles when determining the particle diameter. The $[\Delta\mathrm{L}]$ FWHM was used to determine the particle height.

With the particle dimensions, the degree of truncation determined and used to estimate the adhesion energy of the particles using the Wulff-Kaichew construction. For a free standing isotropic particle the height equals diameter, $H = D$. In the [001] direction, $H = N_B + N_T$ and $N_T = D/2$. In the case of a truncated particle, with Δh describing the degree of truncation and defined as $N_B = N_T - \Delta h$. By comparing a free standing isotropic particle with a truncated particle, the degree of truncation is given by $\Delta h = D - H$ and therefore $N_B = D/2 - (D - H)$.

The normalized intensity differences were calculated by normalizing the difference in intensity with the sum of the two for each data point, $(I_1 - I_0)/(I_1 + I_0)$.

Post Experiment *Ex Situ* Characterisation

Scanning electron microscopy (SEM) was performed at the DESY NanoLab[36] after the P23 oxidation experiments. A high resolution field emission SEM was used. It was observed carbon deposited on to the samples from the electron gun in the SEM chamber can poison the reactivity of Pd nanoparticles. Thus, SEM images were taken after the oxidation experiment was performed. The software ImageJ - Fiji Package[50] was used to count the number of

particles, and estimate the particles' size and coverage.

The heterogeneity of the Pd NPs' orientation on the substrate was further investigated in post synchrotron experiments *ex situ* by performing ω-scans at several Bragg reflexes and with high energy X-ray diffraction, Figure S3 and S4 respectively in the Supporting Information. While the Pd nanoparticle ensemble is dominated by a majority of [001] oriented particles, it was observed that there also exist [111] and a variety of [110] oriented particles. The shape response of the Pd[CoC] particles and Pd[R±3.7] particles are the focal point of this work. Grazing incidence in-plane sample rocking scans were performed at DESY NanoLab utilising a Cu K_α lab source. This was done to investigate the existence of particles of different orientations which were not directly scrutinized at P23, see Figure S3 in the Supporting Information. High energy X-ray diffraction, at 73.7 keV was performed *ex situ* at the PETRA III P07 High Energy Materials Science beamline[51] after the oxidation experiments. The high energy XRD patterns were taken with a Perkin Elmer 1621 flat panel detector. A grazing incidence of 0.025° was used for this experiment, Figure S4 in the Supporting Information.

Acknowledgement

We acknowledge DESY (Hamburg, Germany), a member of the Helmholtz Association HGF, for the provision of experimental facilities. Parts of this research were carried out at PETRA III and we would like to thank O. Gutowski for assistance in the use of the P07 beamline. Scanning Electron Microscopy imaging was performed at the DESY NanoLab by A. Jeromin.

Supporting Information Available

Supporting Information is available online. Illustration of coincidence lattice sites of the two different epitaxy types; scans across the Bragg reflex used to determine the particle dimen-

sions; in-plane rotation scans used to investigate heterogeneity in nanoparticle orientation; complementary high energy X-ray scattering data; illustration and discussion of asymmetric truncation rods; further $[\mathrm{H}, \mathrm{K} = 2 - \mathrm{H}]$ line scans performed at different L; fitted pseudo-Voigt parameters the data; AES and LEED of the MgO substrate prior to Pd deposition.

References

1. Henry, C. R. Surface Studies of Supported Model Catalysts. *Surface Science Reports* **1998**, *31*, 231–325.

2. Liu, L.; Corma, A. Metal Catalysts for Heterogeneous Catalysis: From Single Atoms to Nanoclusters and Nanoparticles. *Chemical Reviews* **2018**, *118*, 4981–5079.

3. Somorjai, G. A.; Li, Y. *Introduction to Surface Chemistry and Catalysis, 2nd Edition*; Wiley: Hoboken (New Jersey), 2010.

4. Ziemecki, S. B.; Jones, G. A.; Swartzfager, D. G.; Harlow, R. L.; Faber, J. Formation of Interstitial Palladium-Carbon Phase by Interaction of Ethylene, Acetylene, and Carbon Monoxide with Palladium. *Journal of the American Chemical Society* **1985**, *107*, 4547–4548.

5. Datye, A. K.; Bravo, J.; Nelson, T. R.; Atanasova, P.; Lyubovsky, M.; Pfefferle, L. Catalyst Microstructure and Methane Oxidation Reactivity during the Pd↔PdO Transformation on Alumina Supports. *Applied Catalysis A: General* **2000**, *198*, 179–196.

6. Aytam, H. P.; Akula, V.; Janmanchi, K.; Kamaraju, S. R. R.; Panja, K. R.; Gurram, K.; Niemantsverdriet, J. W. Characterization and Reactivity of Pd/MgO and Pd/γ-Al2O3 Catalysts in the Selective Hydrogenolysis of CCl2F2. *The Journal of Physical Chemistry B* **2002**, *106*, 1024–1031.

7. Hu, G.; Nitze, F.; Gracia-Espino, E.; Ma, J.; Barzegar, H. R.; Sharifi, T.; Jia, X.;

Shchukarev, A.; Lu, L.; Ma, C.; Yang, G.; Wågberg, T. Small Palladium Islands Embedded in Palladium-Tungsten Bimetallic Nanoparticles Form Catalytic Hotspots for Oxygen Reduction. *Nature Communications* **2014**, *5*, 5253.

8. Dann, E. K.; Gibson, E. K.; Blackmore, R. H.; Catlow, C. R. A.; Collier, P.; Chutia, A.; Erden, T. E.; Hardacre, C.; Kroner, A.; Nachtegaal, M.; Raj, A.; Rogers, S. M.; Taylor, S. F. R.; Thompson, P.; Tierney, G. F.; Zeinalipour-Yazdi, C. D.; Goguet, A.; Wells, P. P. Structural Selectivity of Supported Pd Nanoparticles for Catalytic NH_3 Oxidation Resolved Using Combined *Operando* Spectroscopy. *Nature Catalysis* **2019**, *2*, 157–163.

9. Burda, C.; Chen, X.; Narayanan, R.; El-Sayed, M. A. Chemistry and Properties of Nanocrystals of Different Shapes. *Chemical Reviews* **2005**, *105*, 1025–1102.

10. Roldan Cuenya, B.; Behafarid, F. Nanocatalysis: Size- and Shape-Dependent Chemisorption and Catalytic Reactivity. *Surface Science Reports* **2015**, *70*, 135–187.

11. Schalow, T.; Brandt, B.; Starr, D. E.; Laurin, M.; Shaikhutdinov, S. K.; Schauermann, S.; Libuda, J.; Freund, H.-J. Size-Dependent Oxidation Mechanism of Supported Pd Nanoparticles. *Angewandte Chemie International Edition* **2006**, *45*, 3693–3697.

12. Newton, M. A. Dynamic Adsorbate/Reaction Induced Structural Change of Supported Metal Nanoparticles: Heterogeneous Catalysis and Beyond. *Chemical Society Reviews* **2008**, *37*, 2644.

13. Hemmingson, S. L.; Campbell, C. T. Trends in Adhesion Energies of Metal Nanoparticles on Oxide Surfaces: Understanding Support Effects in Catalysis and Nanotechnology. *ACS NANO* **2017**, *11*, 1196–1203.

14. Ahmadi, M.; Mistry, H.; Roldan Cuenya, B. Tailoring the Catalytic Properties of Metal Nanoparticles *via* Support Interactions. *J. of Phys. Chem. Lett.* **2016**, *7*, 3519–3533.

15. Stierle, A.; Gustafson, J.; Lundgren, E. *Surface-Sensitive X-Ray Diffraction across the Pressure Gap*; Springer International Publishing: Cham, 2017; pp 59–87.

16. Nolte, P.; Stierle, A.; Jin-Phillipp, N. Y.; Kasper, N.; Schulli, T. U.; Dosch, H. Shape Changes of Supported Rh Nanoparticles during Oxidation and Reduction Cycles. *Science* **2008**, *321*, 1654–1658.

17. Nolte, P.; Stierle, A.; Kasper, N.; Jin-Phillipp, N. Y.; Reichert, H.; Rühm, A.; Okasinski, J.; Dosch, H.; Schöder, S. Combinatorial High-Energy X-Ray Microbeam Study of the Size-Dependent Oxidation of Pd Nanoparticles on MgO(100). *Physical Review B* **2008**, *77*, 115444.

18. Hejral, U.; Vlad, A.; Nolte, P.; Stierle, A. *In Situ* Oxidation Study of Pt Nanoparticles on MgO(001). *The Journal of Physical Chemistry C* **2013**, *117*, 19955–19966.

19. Gustafson, J.; Shipilin, M.; Zhang, C.; Stierle, A.; Hejral, U.; Ruett, U.; Gutowski, O.; Carlsson, P.-A.; Skoglundh, M.; Lundgren, E. High-Energy Surface X-Ray Diffraction for Fast Surface Structure Determination. *Science* **2014**, *343*, 758–761.

20. Hejral, U.; Franz, D.; Volkov, S.; Francoual, S.; Strempfer, J.; Stierle, A. Identification of a Catalytically Highly Active Surface Phase for CO Oxidation over PtRh Nanoparticles under *Operando* Reaction Conditions. *Physical Review Letters* **2018**, *120*, 126101.

21. Kawaguchi, T.; Keller, T. F.; Runge, H.; Gelisio, L.; Seitz, C.; Kim, Y. Y.; Maxey, E. R.; Cha, W.; Ulvestad, A.; Hruszkewycz, S. O.; Harder, R.; Vartanyants, I. A.; Stierle, A.; You, H. Gas-Induced Segregation in Pt-Rh Alloy Nanoparticles Observed by *in Situ* Bragg Coherent Diffraction Imaging. *Physical Review Letters* **2019**, *123*, 246001.

22. Abuin, M.; Kim, Y. Y.; Runge, H.; Kulkarni, S.; Maier, S.; Dzhigaev, D.; Lazarev, S.; Gelisio, L.; Seitz, C.; Richard, M.-I.; Zhou, T.; Vonk, V.; Keller, T. F.; Vartanyants, I. A.; Stierle, A. Coherent X-Ray Imaging of CO-Adsorption-Induced Structural Changes in

Pt Nanoparticles: Implications for Catalysis. *ACS Applied Nano Materials* **2019**, *2*, 4818–4824.

23. Wulff, G. XXV. Zur Frage der Geschwindigkeit des Wachsthums und der Auflösung der Krystallflächen. *Zeitschrift für Kristallographie - Crystalline Materials* **1901**, *34*.

24. Barmparis, G. D.; Lodziana, Z.; Lopez, N.; Remediakis, I. N. Nanoparticle Shapes by Using Wulff Constructions and First-Principles Calculations. *Beilstein Journal of Nanotechnology* **2015**, *6*, 361–368.

25. Henry, C. Morphology of Supported Nanoparticles. *Porgress in Surface Science* **2005**, *80*, 92–116.

26. Graoui, H.; Giorgio, S.; Henry, C. Shape Variations of Pd Particles under Oxygen Adsorption. *Surface Science* **1998**, *417*, 350–360.

27. Renaud, G. Real-Time Monitoring of Growing Nanoparticles. *Science* **2003**, *300*, 1416–1419.

28. Kasper, N.; Stierle, A.; Nolte, P.; Jin-Phillipp, Y.; Wagner, T.; de Oteyza, D.; Dosch, H. *In Situ* Oxidation Study of MgO(100) Supported Pd Nanoparticles. *Surface Science* **2006**, *600*, 2860–2867.

29. Olander, J.; Lazzari, R.; Jupille, J.; Mangili, B.; Goniakowski, J.; Renaud, G. Size- and Temperature-Dependent Epitaxy for a Strong Film-Substrate Mismatch: The Case of Pt/MgO(001). *Physical Review B* **2007**, *76*, 075409.

30. Cuenya, B. R. Synthesis and Catalytic Properties of Metal Nanoparticles: Size, Shape, Support, Composition, and Oxidation State Effects. *Thin Solid Films* **2010**, *518*, 3127–3150.

31. van Deelen, T. W.; Mejia, C. H.; de Jong, K. P. Control of Metal-Support Interactions

in Heterogeneous Catalysts to Enhance Activity and Selectivity. *Nature Catalysis* **2019**, *2*, 955–970.

32. Mittendorfer, F.; Seriani, N.; Dubay, O.; Kresse, G. Morphology of Mesoscopic Rh and Pd Nanoparticles under Oxidizing Conditions. *Physical Review B* **2007**, *76*, 233413.

33. Nolte, P.; Stierle, A.; Kasper, N.; Jin-Phillipp, N. Y.; Jeutter, N.; Dosch, H. Reversible Shape Changes of Pd Nanoparticles on MgO(100). *Nano Letters* **2011**, *11*, 4697–4700.

34. Westerström, R.; Gustafson, J.; Resta, A.; Mikkelsen, A.; Andersen, J. N.; Lundgren, E.; Seriani, N.; Mittendorfer, F.; Schmid, M.; Klikovits, J.; Varga, P.; Ackermann, M. D.; Frenken, J. W. M.; Kasper, N.; Stierle, A. Oxidation of Pd(553): From Ultrahigh Vacuum to Atmospheric Pressure. *Physical Review B* **2007**, *76*, 155410.

35. Vlad, A.; Stierle, A.; Westerström, R.; Blomberg, S.; Mikkelsen, A.; Lundgren, E. Oxygen Interaction with the Pd(112) Surface: From Chemisorption to Bulk Oxide Formation. *Physical Review B* **2012**, *86*, 035407.

36. Stierle, A.; Keller, T. F.; Noei, H.; Vonk, V.; Roehlsberger, R. DESY NanoLab. *Journal of large-scale research facilities JLSRF* **2016**, *2*, A76.

37. Lundgren, E.; Gustafson, J.; Mikkelsen, A.; Andersen, J. N.; Stierle, A.; Dosch, H.; Todorova, M.; Rogal, J.; Reuter, K.; Scheffler, M. Kinetic Hindrance during the Initial Oxidation of Pd(100) at Ambient Pressures. *Physical Review Letters* **2004**, *92*, 046101.

38. Winterbottom, W. Equilibrium Shape of a Small Particle in Contact with a Foreign Substrate. *Acta Metallurgica* **1967**, *15*, 303–310.

39. Seriani, N.; Mittendorfer, F. Platinum-Group and Noble Metals under Oxidizing Conditions. *Journal of Physics: Condensed Matter* **2008**, *20*, 184023.

40. Vervisch, W.; Mottet, C.; Goniakowski, J. Effect of Epitaxial Strain on the Atomic

Structure of Pd Clusters on MgO(100) Substrate. *The European Physical Journal D - Atomic, Molecular and Optical Physics* **2003**, *24*, 311–314.

41. Graoui, H.; Giorgio, S.; Enry, C. R. Effect of the Interface Structure on the High-Temperature Morphology of Supported Metal Clusters. *Philosophical Magazine B* **2001**, *81*, 1649–1658.

42. Renaud, G.; Barbier, A.; Robach, O. Growth, Structure, and Morphology of the Pd/MgO(001) Interface: Epitaxial Site and Interfacial Distance. *Physical Review B* **1999**, *60*, 5872–5882.

43. Robinson, I.; Harder, R. Coherent X-Ray Diffraction Imaging of Strain at the Nanoscale. *Nature Materials* **2009**, *8*, 291–298.

44. Karpov, D.; Fohtung, E. Bragg Coherent Diffractive Imaging of Strain at the Nanoscale. *Journal of Applied Physics* **2019**, *125*, 121101.

45. Chang, S.; Thiel, P. A. Oxygen on Pd(100): Order, Reconstruction, and Desorption. *The Journal of Chemical Physics* **1988**, *88*, 2071–2082.

46. Todorova, M.; Lundgren, E.; Blum, V.; Mikkelsen, A.; Gray, S.; Gustafson, J.; Borg, M.; Rogal, J.; Reuter, K.; Andersen, J.; Scheffler, M. The Pd(100)-($\sqrt{5} \times \sqrt{5}$)R27°-O Surface Oxide Revisited. *Surface Science* **2003**, *541*, 101–112.

47. Kasper, N.; Nolte, P.; Stierle, A. Stability of Surface and Bulk Oxides on Pd(111) Revisited by *in Situ* X-Ray Diffraction. *The Journal of Physical Chemistry C* **2012**, *116*, 21459–21464.

48. Westerström, R.; Weststrate, C. J.; Gustafson, J.; Mikkelsen, A.; Schnadt, J.; Andersen, J. N.; Lundgren, E.; Seriani, N.; Mittendorfer, F.; Kresse, G.; Stierle, A. Lack of Surface Oxide Layers and Facile Bulk Oxide Formation on Pd(110). *Physical Review B - Condensed Matter and Materials Physics* **2009**, *80*, 1–11.

49. Hejral, U.; Müller, P.; Shipilin, M.; Gustafson, J.; Franz, D.; Shayduk, R.; Rütt, U.; Zhang, C.; Merte, L. R.; Lundgren, E.; Vonk, V.; Stierle, A. High-Energy X-Ray Diffraction from Surfaces and Nanoparticles. *Physical Review B* **2017**, *96*, 195433.

50. Schindelin, J.; Arganda-Carreras, I.; Frise, E.; Kaynig, V.; Longair, M.; Pietzsch, T.; Preibisch, S.; Rueden, C.; Saalfeld, S.; Schmid, B.; Tinevez, J.-Y.; White, D. J.; Hartenstein, V.; Eliceiri, K.; Tomancak, P.; Cardona, A. Fiji: An Open-Source Platform for Biological-Image Analysis. *Nature Methods* **2012**, *9*, 676–682.

51. Schell, N.; King, A.; Beckmann, F.; Fischer, T.; Müller, M.; Schreyer, A. The High Energy Materials Science Beamline (HEMS) at PETRA III. *Materials Science Forum* **2013**, *772*, 57–61.